Bioresource Technology 132 (2013) 254–261

Contents lists available at SciVerse ScienceDirect

Bioresource Technology

journal homepage: www.elsevier.com/locate/biortech

# Preparation of highly porous binderless activated carbon electrodes from fibres of oil palm empty fruit bunches for application in supercapacitors

R. Farma [a,b], M. Deraman [a,*], A. Awitdrus [a,b], I.A. Talib [a], E. Taer [a,b], N.H. Basri [a], J.G. Manjunatha [a], M.M. Ishak [a], B.N.M. Dollah [a], S.A. Hashmi [c]

[a] School of Applied Physics, Faculty of Science and Technology, Universiti Kebangsaan Malaysia, 43600 Bangi, Selangor, Malaysia
[b] Department of Physics, Faculty of Mathematics and Natural Sciences, University of Riau, 28293 Pekanbaru, Riau, Indonesia
[c] Department of Physics and Astrophysics, University of Delhi, Delhi 110007, India

## HIGHLIGHTS

- Oil palm empty fruit bunches have been processed into supercapacitor electrodes.
- $CO_2$ and KOH activations can produce highly porous binderless carbon electrodes.
- Small quantity KOH can reduce $CO_2$ activation time significantly.
- Supercapacitors based on these electrodes exhibit excellence performances.
- Therefore this novel method offers a significant economic advantage.

## ARTICLE INFO

*Article history:*
Received 28 September 2012
Received in revised form 4 January 2013
Accepted 6 January 2013
Available online 22 January 2013

*Keywords:*
Biomass
Chemical activation
Physical activation
Activated carbon electrode
Supercapacitor

## ABSTRACT

Fibres from oil palm empty fruit bunches, generated in large quantities by palm oil mills, were processed into self-adhesive carbon grains (SACG). Untreated and KOH-treated SACG were converted without binder into green monolith prior to $N_2$-carbonisation and $CO_2$-activation to produce highly porous binderless carbon monolith electrodes for supercapacitor applications. Characterisation of the pore structure of the electrodes revealed a significant advantage from combining the chemical and physical activation processes. The electrochemical measurements of the supercapacitor cells fabricated using these electrodes, using cyclic voltammetry, electrochemical impedance spectroscopy and galvanostatic charge–discharge techniques consistently found that approximately 3 h of activation time, achieved via a multi-step heating profile, produced electrodes with a high surface area of 1704 $m^2 g^{-1}$ and a total pore volume of 0.889 $cm^3 g^{-1}$, corresponding to high values for the specific capacitance, specific energy and specific power of 150 F $g^{-1}$, 4.297 Wh $kg^{-1}$ and 173 W $kg^{-1}$, respectively.



## 1. Introduction

Supercapacitors are electrochemical devices that primarily consist of electrodes, current collectors, an electrolyte and a spacer and are promising electrical energy storage devices for applications that demand high energy density, high reliability, maximum power, long-cycle life or long-term operation stability, suitable dimensions and weight, low cost, fast discharge/charge time, low level of heating, safety, etc. Its energy capacities allow supercapacitors to fill the gap between batteries and conventional capacitors in term of energy and power requirements. Therefore, applications of supercapacitors include in appliances such as electronic devices, electric vehicles, and military equipment.

Common materials used as supercapacitor electrodes include conducting polymers, metal oxides, and porous materials such as activated carbon, carbon aerogels and carbon nanotubes. Activated carbon is advantageous because of its high surface area and porosity, good thermal and electrical conductivity, good anti-causticity, high stability, low cost and commercial-scale availability (Pandolfo and Hollenkamp, 2006; Obreja, 2008).

Activated carbon electrodes can be produced from biomass precursors (wood, fruit shells, stones and bunches) and fossil-fuel based precursors (petroleum and coal) and have been tested for supercapacitor applications. Biomass precursors are cheaper, readily available, environmentally friendly, renewable, and structurally porous.

The palm oil industry is a major agricultural sector in Malaysia, Indonesia and Thailand, covering 27 million hectares of agricultural land. This industry involves the processing of oil palm fruits

* Corresponding author. Tel.: +60 387366373; fax: +60 389213777.
*E-mail address:* madra@pkrisc.cc.ukm.my (M. Deraman).

0960-8524/$ - see front matter © 2013 Elsevier Ltd. All rights reserved.
http://dx.doi.org/10.1016/j.biortech.2013.01.044

into cooking oil and generates large quantities of biomass waste that are a pollutant if directly discharged into the environment. This biomass waste includes palm kernel cakes, palm kernel shells, empty fruit bunches (EFB) and mesocarp fibres (Razuan et al., 2010; Fan et al., 2011). In Malaysia, the annual production of EFB is 8.5 million tons and is traditionally used as fertiliser (after burning), mulching material for palm oil plantations and boiler fuel in palm oil mills. Non-traditional uses include bedding material, particleboard and medium density fibreboard. In the present study, EFB has been used as a raw material to produce monolithic nanoporous activated carbon for supercapacitor electrodes. The processing of EFB involves pre-carbonisation, pulverisation, pelletisation, chemical treatment, carbonisation and activation. The amounts of chemical activating agent (KOH) used for the treatment of pre-carbonised EFB were appropriately selected, and the activation time was varied to control development of the electrode pore structure. The symmetrical supercapacitor cells were fabricated using these electrodes and the capacitive behaviour of the electrodes and their supercapacitor performance was evaluated using electrochemical methods including cyclic voltammetry (CV), electrochemical impedance spectroscopy (EIS) and galvanostatic charge–discharge (GCD). The objective of this paper is to investigate the relationship of the behaviour and performance of supercapacitor cells to the pore-structure of electrodes especially as it relates to the activation time during electrode preparation.

## 2. Experimental

### 2.1. Electrode preparation and cell fabrication

Self-adhesive carbon grains (SACG) were prepared from fibres of EFB using our previously reported method (Deraman et al., 1998). The method begins with the pre-carbonisation of fibres of EFB at low temperature (~280 °C), followed by ball milling for approximately 18 h, and sieving to obtain a powder of SACG with a particle size of <106 μm. The SACG was mixed with KOH at a ratio (by weight) of 5% KOH to 95% SACG. The wet mixing was conducted in distilled water, and the mixture was stirred for ~1 h to ensure homogeneity, followed by drying and milling for 20 min to produce a fine powder of KOH-treated SACG. Green monoliths (GMs) of the SACG and green monolith (GMK) of the KOH-treated SACG were prepared in a mould (20 mm diameter) using 250 kg $cm^{-2}$ of compression force. The materials were carbonised at ~800 °C under a $N_2$ atmosphere (with a flow rate of 1.5 litres per minute) to produce the carbon monoliths (CM), carbon monolith of the untreated SACG (CM-U) and carbon monolith of the treated SACG (CM-K). The CM-U and CM-K were activated by $CO_2$ (with a flow rate of 1 litre per minute) from room temperature to ~800 °C at a rate of 5 °C per minute to produce the activated carbon monoliths (ACM), ACM-U and ACM-K.

ACM-U and ACM-K were produced by $CO_2$ activation at several activation times, i.e., 1, 2, 3, 4 and 5 h. To avoid cracks due to excessive heating after activation longer than 2 h, a multi-step activation method which divided the total activation time into several segments of heating steps, previously employed by us (Taer et al., 2010), was used in this study. For convenience, the ACMs produced are labelled as ACM-U1 to ACM-U5 and ACM-K1 to ACM-K5 to denote activation times of 1–5 h, respectively. All ACM electrode, after polished into the required thickness (~0.4 mm), were washed to remove the activating agent with distilled water until pH 7. The electrodes were found to decrease slightly in weight after washing.

For studying the capacitive properties of the ACMs electrodes, symmetrical supercapacitor cells were fabricated using two ACMs electrodes prepared for each selected activation time. Stainless steel foils (316-L stainless steel foils with a thickness 0.02 mm, Goodfellow Cambridge Ltd., England) were used as the current collectors and 1 M sulphuric acid was used as an electrolyte. A Teflon spacer ring separated the ACM electrodes by 0.2 mm. The diameter, thickness and weight of the ACM electrodes were ~14.5 mm, ~0.4 mm and 50–60 mg, respectively.

### 2.2. Physical characterisation

The dimension and weight of the ACMs were measured to determine the sample density. The porosity parameters of the ACMs (i.e., Brunauer–Emmett–Teller (BET) surface area ($S_{BET}$), mesopore surface area ($S_{Meso}$), micropore volume ($V_{Micro}$), total pore volume ($V_{Tot}$) and average pore diameter ($D$)) were determined from nitrogen adsorption–desorption isotherm data recorded at −196 °C using an Accelerated Surface Area and Porosimeter system (ASAP 2010, Micromeritics). The calculation of these parameters was done based on the standard method (Sing et al., 1985). The structural features of the ACMs were investigated by X-ray diffraction (XRD). XRD patterns were generated over a diffraction angle ($2\theta$) range from 5° to 85°, using a Bruker AXS D8 advance diffractometer that employed $CuK_\alpha$ radiation. The interlayer spacing ($d_{002}$) of the ACMs was evaluated by the application of Bragg's Law ($n\lambda = 2d \sin 2\theta$) to the position of the (002) peak, where $n = 1$ and $\lambda = 1.5406$ Å. The microcrystallite dimension (stack height = $L_c$, stack width = $L_a$) of the ACMs was calculated from the XRD diffraction pattern using the Debye–Scherrer equations ($L_c = 0.89\lambda/\beta\cos(\theta_{002})$ and $L_a = 1.94\lambda/\beta\cos(\theta_{100})$, where $\beta$ is equal to the peak width at half height (Carrott et al., 2001; Awitdrus et al., 2010; Valante-Nabais et al., 2011) of the respective peaks. The morphology of the ACMs was investigated using a Field Emission Scanning Electron Microscopy (FESEM) technique (Supra PV 55 model).

### 2.3. Electrochemical characterisation

An electrochemical instrument (Solartron 1286 electrochemical interface and Solartron 1255 HF frequency response analyser) was used to study the performance of the supercapacitor cells using CV, EIS and GCD methods. All measurements were carried out at room temperature (25 °C). From the voltammogram, the specific capacitance ($C_{sp}$) of the electrodes was determined using equation:

$$C_{sp} = \frac{2i}{Sm} \quad (1)$$

where $i$ = electric current, $S$ = scan rate and $m$ = weight of electrode.

From the EIS data, the specific capacitance ($C_{sp}$) of the electrodes was determined using equation:

$$C_{sp} = -\frac{1}{\pi f Z'' m} \quad (2)$$

where $f$ = frequency, and $Z''$ = imaginary impedance at $f$. The EIS data as a function of the frequency were analysed using the following equations:

$$C(\omega) = C'(\omega) - jC''(\omega) \quad (3)$$

$$C''(\omega) = -Z'(\omega)/\omega|Z(\omega)|^2 \quad (4)$$

$$C'(\omega) = Z^{Prime}(\omega)/\omega|Z(\omega)|^2 \quad (5)$$

where $Z(\omega) = 1/j\omega C(\omega)$, $C'$ = real capacitance, $C''$ = imaginary capacitance, $Z'$ = real impedance, and $Z''$ = imaginary impedance (Portet et al., 2005).

From the GCD data (charge–discharge curve) recorded at a current density of 10 mA $cm^{-2}$, the specific capacitance ($C_{sp}$) of the electrodes was determined using equation:

$$C_{sp} = \frac{2i}{(\frac{\Delta V}{\Delta t})m} \quad (6)$$

where $i$ = discharge current, $\Delta t$ = discharge time, and $\Delta V$ = voltage (Beidaghi et al., 2011; Tsay et al., 2012; Valante-Nabais et al., 2011; Elmouwahidi et al., 2012). Also from the GCD data, the values of the specific power ($P$) and specific energy ($E$) were calculated using equations below, respectively:

$$P = \frac{V_i}{m} \quad (7)$$

$$E = \frac{Vit}{m} \quad (8)$$

where $i$ = discharge current, $V$ = voltage excluding the iR drop at the beginning of the discharge, and $t$ is time.

## 3. Results and discussion

### 3.1. Physical properties

#### 3.1.1. Weight, dimension and density

The average weight ($w$), thickness ($t$), diameter ($d$) and density ($\rho$) from the 10 duplicate samples of the ACM-Us and ACM-Ks were recorded before and after $CO_2$ activation with different activation times. The values of these parameters decrease after $CO_2$ activation for the both ACM-Us and ACM-Ks (not shown here) due to weight loss and volume shrinkage. The weight loss is associated with the release of carbon atoms resulting from reaction with $CO_2$, and the volume shrinkage is associated with the rearrangement of carbon atoms during activation. To illustrate the effect of varying activation time on the weight, dimensional and density changes of the samples, a plot of the percentages of weight loss, dimensional shrinkage and density decrease after activation is shown in Fig. 1. ACM-K3 clearly exhibits the highest percent change.

#### 3.1.2. X-ray diffraction and crystallite dimension

X-ray diffractograms for all of the ACM-Ks electrodes (not shown here) show a similar diffraction pattern, with two broad peaks common for carbon materials appear at diffraction angles of approximately 24° and 44°, due to reflections from the (002) and (100) planes, respectively. This similarity indicates that all the electrodes are in a semicrystalline form, in which the building blocks are made of microcrystallites that are randomly oriented and distributed throughout the samples. A turbostratic model has been successfully used to describe the structure of different types of semicrystalline carbon samples (Coutinho et al., 2000; Deraman et al., 2002; Awitdrus et al., 2010). A sharp peak at $2\theta$ = 26.48 is due to a very small amount of silica material (JCPDS Card No. 89-1668) in the ACM-K electrodes.

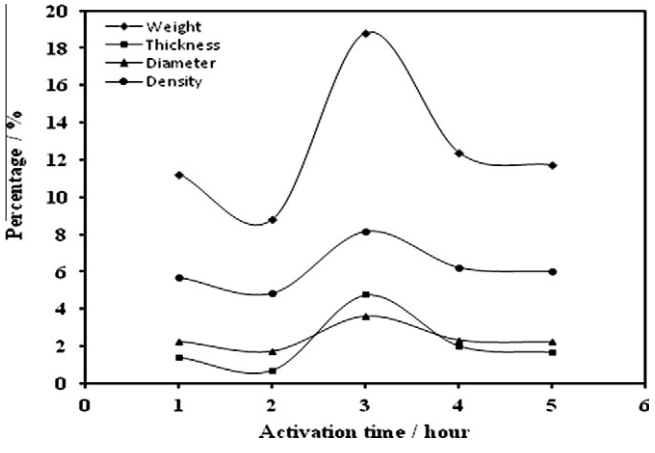


Fig. 1. Percentages of weight loss, dimensional shrinkage and density decrease

The structural parameters, i.e., the interlayer spacing ($d_{002}$) and microcrystallites dimensions ($L_c$ and $L_a$) were calculated from the X-ray diffraction data and are given in Table 1. These data fall within the typical range of values for carbon material. For example, the values of $d_{002}$, $L_c$ and $L_a$ in the ranges of 3.532–3.608 Å, 8.433–19.217 Å and 15.384–43.321 Å, respectively, were reported for the carbon electrode from a mixture of fibres of EFB and green petroleum cokes (Awitdrus et al., 2010). Activated carbon from a coffee endocarp precursor demonstrated a $d_{002}$ between 3.04 and 3.84 Å, a $L_c$ between 10.3 and 14.1 Å, and a $L_a$ between 23.3 and 38.2 Å (Valante-Nabais et al., 2011).

The change in $d_{002}$ value was very small and does not show a general trend that correlates with the changes in activation time (Table 1). In general, $d_{002}$ strongly depends on the activation temperature (Coutinho et al., 2000). In the present study, the activation time was varied at a fixed activation temperature, and it was therefore expected that the longer activation time would not significantly affect the position of the 002 diffraction peak or the $d_{002}$ value. However, the 002 peak broadening seems to vary with the activation time. It is well known that the broader the peak, the smaller is the microcrystallite size (Coutinho et al., 2000; Valante-Nabais et al., 2011). The data in Table 1 clearly indicate that microcrystallites in ACMs change in their stack height ($L_c$) and stack width ($L_a$), and the results in this table can be further analysed in term of the ratios $L_c/d_{002}$ and $L_c/L_a$. The former ratio represents the mean number of planes in the microcrystallites ($N_p$), and the latter ratio represents the relative density of the edge and basal planes in microcrystallites, a measure of their edge orientation. The ratios of $L_c/d_{002}$ and $L_c/L_a$ are analysed against the activation time and both ratios show similar behaviour with the presence of the highest peak values at the activation time of 3 h, respectively. It will be shown below that this behaviour is associated with the development of electrode pore structures and can therefore influence the formation of the electric double layer and capacitance of the electrodes.

The empirical formula that relates the stack height of microcrystallite ($L_c$), surface area ($S$) and density ($\rho$) is given by $S = \frac{2}{\rho L_c}$ and has been used in studies of carbon electrodes from viscose rayon cloth (Kumar et al., 1997). In the present study, $L_c$ appears to increase with activation time, contrary to the above formula. It has been observed elsewhere that as the activation time increases, the microcrystallite stack and width and the interlayer spacing also tend to decrease (Coutinho et al., 2000). This trend differs from our data because the precursors and method of carbon production were different.

#### 3.1.3. Nitrogen adsorption and desorption

Fig. 2 shows nitrogen adsorption–desorption isotherms for the ACM-U1 and ACM-K1 to ACM-K5 electrodes recorded at −196 °C. All of the isotherms exhibit a similar pattern, showing a combination of types I and IV shaped according to IUPAC classification (Sing et al., 1985; Chen et al., 2012), which indicate that all the electrodes are porous carbon material containing both micropores

**Table 1**
Interlayer spacing, crystallite dimension, and ratios of $L_c/L_a$ and $L_c/d_{002}$ for ACM-Ks.

| Cells | $d_{002}$ (Å) | $d_{100}$ (Å) | $L_c$ (Å) | $L_a$ (Å) | $L_c/L_a$ | $L_c/d_{002}$ |
|---|---|---|---|---|---|---|
| ACM-K1 | 3.711 | 2.068 | 9.50 | 52.81 | 0.180 | 2.560 |
| ACM-K2 | 3.692 | 2.039 | 10.09 | 51.77 | 0.195 | 2.733 |
| ACM-K3 | 3.701 | 2.035 | 10.48 | 48.33 | 0.217 | 2.832 |
| ACM-K4 | 3.695 | 2.062 | 9.05 | 49.73 | 0.182 | 2.450 |
| ACM-K5 | 3.699 | 2.086 | 8.47 | 52.22 | 0.162 | 2.290 |

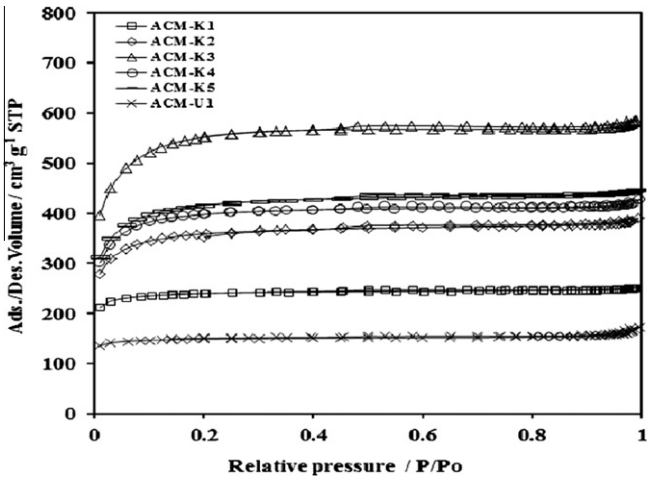


**Fig. 2.** Nitrogen adsorption–desorption isotherms of ACM-U1 and the ACM-Ks.

and mesopores, with high internal surface area. A comparison between the isotherms for the ACM-U1 and ACM-K1 electrodes clearly shows that the use of 5% KOH can significantly enhance the adsorption capacity of the electrodes. This enhancement is maximal for electrodes prepared with 3 h of activation time, as shown by the isotherms of ACM-K2 to ACM-K5 (Fig. 2). A quantitative interpretation of the isotherms shown in Fig. 2 is shown in Table 2, in terms of pore structure characteristics including $S_{BET}$, $S_{meso}$, $V_{total}$, $V_{micro}$ and $D$. A comparison of the results clearly shows the effect of combining KOH activation and $CO_2$ activation at activation times from 1 to 5 h.

Activated carbon from sunflower seed shells prepared by KOH activation has an $S_{BET}$ of 619–1235 $m^2 g^{-1}$, whereas activated carbon from the same precursor prepared via the combination of chemical activation (KOH) and physical activation ($CO_2$) has larger $S_{BET}$ values, i.e., 936–2585 $m^2 g^{-1}$ (Li et al., 2011). These results show that the combined activation approach can improve activation by a factor of 51–109%. In our study, a comparison between ACM-U1 and ACM-K1 reveals a similar improvement, as shown in Table 2. The combined activation approach gives higher $S_{BET}$ values. Another similarly high $S_{BET}$ value can be observed for carbon electrodes prepared by the same approach from cassava peel wastes i.e., 1352 $m^2 g^{-1}$ (Ismanto et al., 2010). This improvement can be explained by the activation mechanism for KOH at high temperature (800 °C); the reaction between KOH and carbon produces metallic potassium. The interaction of metallic potassium in the carbon matrix can widen the space between carbon atomic layers and lead to an increase in total pore volume. At such an activation temperature, surface metal complexes are formed and can create further gasification that widens micropores to mesopores. The extension of activation time allowed this beneficial process to occur over a longer duration, and the sample concurrently benefited from the effect of $CO_2$ activation. The mechanism of $CO_2$ activation can be found elsewhere (Zhao et al., 2007). This double effect is clearly revealed by Table 2, i.e., $S_{meso}/S_{micro}$ = 0.14, 0.16, 0.40 and 0.46 for the samples ACM-U1, ACM-K1, ACM-K2 and ACM-K3, respectively.

**Table 2**
Pore characteristic parameter values for ACM-U1 and ACM-Ks.

| Samples | ACM-U1 | ACM-K1 | ACM-K2 | ACM-K3 | ACM-K4 | ACM-K5 |
|---|---|---|---|---|---|---|
| $S_{BET}$ ($m^2 g^{-1}$) | 448 | 723 | 1100 | 1704 | 1219 | 1279 |
| $S_{Meso}$ ($m^2 g^{-1}$) | 55 | 98 | 315 | 539 | 280 | 413 |
| $V_{total}$ ($cm^3 g^{-1}$) | 0.26 | 0.39 | 0.60 | 0.89 | 0.65 | 0.69 |
| $V_{Micro}$ ($cm^3 g^{-1}$) | 0.21 | 0.33 | 0.42 | 0.62 | 0.50 | 0.46 |
| $D$ (nm) | 2.29 | 2.15 | 2.16 | 2.24 | 2.13 | 2.15 |

The mesopore to micropore volume ratio shows that longer activation times caused a greater increase in the volume of mesopores. Both micropores and mesopores are important for electrode applications because they have different roles with respect to fast charge transfer and the double layer formation of electrolyte ions in the networks of electrode pores (Simon and Gogotsi, 2008; Zhang and Zhao, 2009).

### 3.2. Electrochemical properties

#### 3.2.1. Cyclic voltammetry

CV at a scan rate of 1 mV $s^{-1}$ for all cells fabricated using ACM-U electrodes with various activation time was performed, and the results are shown in Fig. 3(a). In the middle potential region of the voltammograms, there are rectangular windows with no distinct peaks, indicating the absence of strong pseudocapacitive (faradaic) phenomena. In other words, the charge–discharge responses of all of the cells are almost purely electrostatic. The window area is broader for electrodes with higher activation times, indicating that increasing activation time may help to increase the specific capacitance of the electrodes. It has also been noted that the positive branch of the cyclic voltammogram (Fig. 3(a)) is less horizontal than the corresponding negative branch. This suggests that the charging of electrodes with anions $(SO_4)^{2-}$ produces a steady state that is more dependent on the electrical potential than charging with cations ($H^+$). This behaviour is more apparent for electrodes prepared with longer activation times and contributes more to the lack of symmetry in the shape of the CV responses. The time taken to achieve an almost positive steady state current appears to vary with the activation time, suggesting that for all cells, anionic and cationic charging/discharging processes become more potential-dependent as the activation time increases. This is evident in the larger deviation of current responses from a perfect horizontal line.

Fig. 3(b) shows the cyclic voltammograms for all of the cells fabricated using ACM-K electrodes prepared with varying activation times. The pattern of voltammograms is similar to Fig. 3(a). The window area progressively increases with activation time: each window area in Fig. 3(b) is larger than the corresponding area in Fig. 3(a), indicating the significant positive effect of combined KOH–$CO_2$ activation to improve electrode performance. A noticeable feature is that the ACM-K electrode with one hour activation time can achieve approximately the same performance as the ACM-U electrode with 5 h activation. This difference indicates a significant role for the incorporation of KOH in the green monolith prior to the carbonisation step, which is then followed by the activation step.

The rate capability of the cells to store charges can be analysed from the cyclic voltammograms produced over a range of scan rates. This analysis was performed for all of the ACM-U and ACM-K based cells, and the results indicate that for all activation times, the area of the rectangular window increases with the scan rate from 1 to 100 mV $s^{-1}$, indicating that the charge/discharge performances of these electrodes is markedly time-dependent. In all cases, the increase in area under the voltammograms was observed without any major distortion of the rectangular window, indicating that these electrodes exhibit typical capacitive behaviour with good reversibility and high stability for scan rates from 1 to100 mV $s^{-1}$. To illustrate their similar features, Fig. 3(c) shows the plot for the ACM-K3 cell over such a range of scan rates. For lower scan rates from 1 to 25 mV $s^{-1}$, the electrodes seem to maintain the potential region for steady-state current density, indicating that electrodes have better capacitive behaviour than at higher scan rates (e.g., 50 and 100 mV $s^{-1}$), for which the data tend to exhibit more sloping branches on both the negative and positive sides. Such a minor distortion from the ideal rectangular shape

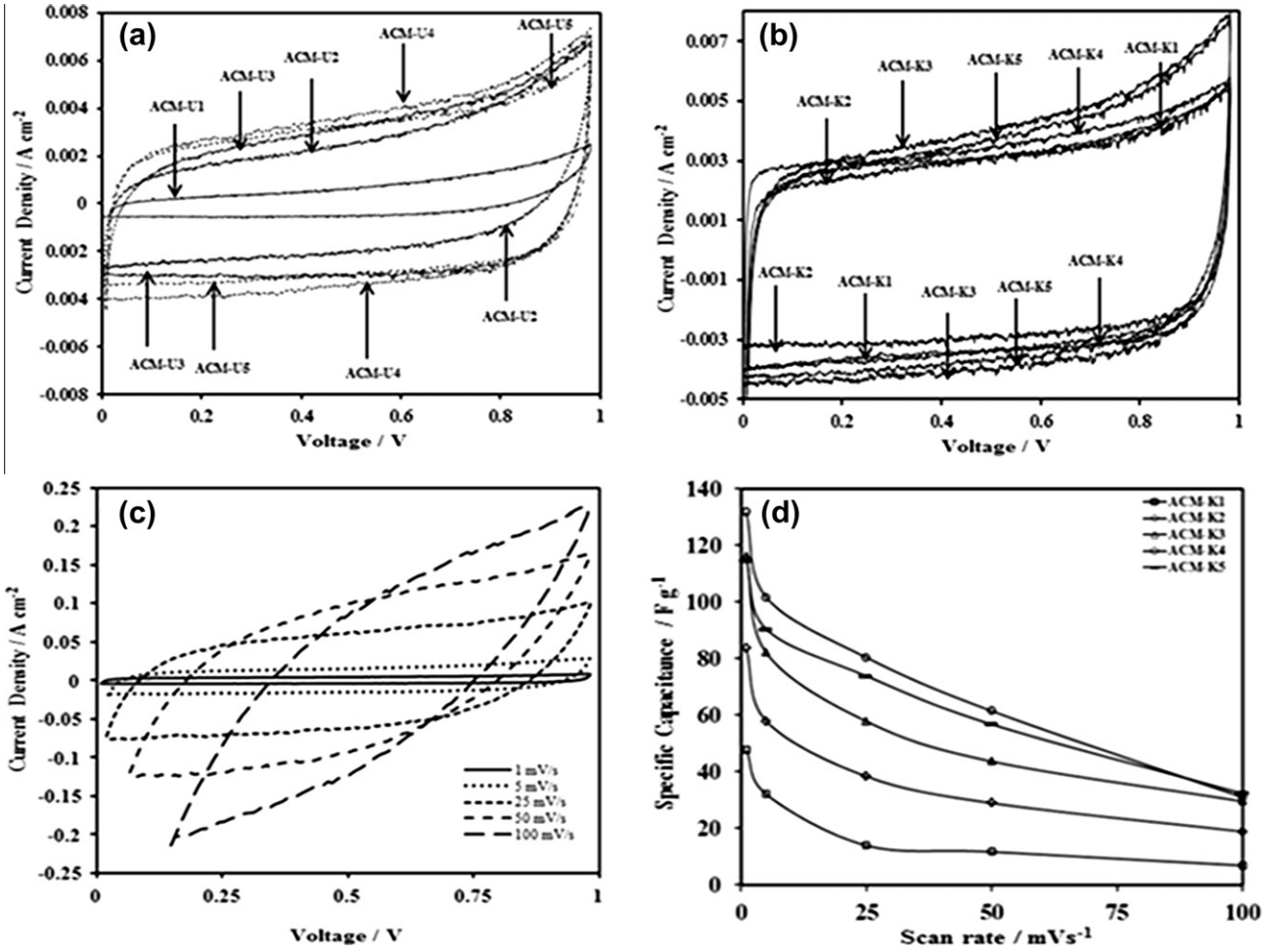


**Fig. 3.** CV data obtained at a scan rate of 1 $mVs^{-1}$ for (a) ACM-Us cells and (b) ACM-Ks cells, (c) for ACM-K3 with various scan rates, and (d) specific capacitance vs. scan rate from CV data of ACM-K-based capacitor cells.

indicates that the capacitive behaviour of the electrode material is weaker, which is typical for porous electrode materials with almost ideal polarisable characteristics (Valante-Nabais et al., 2011).

The $C_{sp}$ can be determined from the measured current intensity ($i$) and scan rate ($S$) using Eq. (1). Fig. 3(d) shows the $C_{sp}$ values determined at different scan rates for all ACM-K-based cells. $C_{sp}$ decreases with an increasing scan rate due to the diffusion limit of the pores. The electrodes prepared with higher activation times showed higher $C_{sp}$ than did lower activation times, which is attributed to the development of fewer small pores in the ACM-K1 electrodes. This indicates that optimisation of the activation time can improve electrode performance. The highest $C_{sp}$ is that of the ACM-K3 electrode, suggesting that 3 h of activation time is the optimum duration. The reduction of $C_{sp}$ is drastic at very low scan rates (below ~5 mV $s^{-1}$); thereafter, gradual decreases were noted with increasing scan rates until a maximum reduction in the scan rate was reached at 100 mV $s^{-1}$ for all of the ACMK cells. It should be noted that high, constant $C_{sp}$ is needed at each scan rate for the fabrication of efficient supercapacitors (Lin et al., 2009). Under these conditions, the porous electrode does not have a constant electric potential and therefore causes a dispersion of capacitance and the degradation of electrical properties such as the rate of charge and discharge.

### 3.2.2. Electrochemical impedance spectroscopy

EIS data expressed in the typical Nyquist plots for the ACM-U and ACM-K supercapacitor cells are given in Fig. 4(a and b), respectively. The Nyquist plot for all of the cells consist of a relatively large semicircle in the high-frequency region, followed by a straight line segment with a slope near 45° in the intermediate frequency range (199.526–0.316 Hz) and another steeply rising straight line segment as the impedance data approached the low-frequency region (0.316–0.01 Hz). The semicircle in Fig. 4(a and b) represents a combination of responses from both the major resistive effect and a very minor capacitive effect at the electrode/solution interface. The resistive response arises from several effects including the electronic resistance of the electrodes, interfacial resistance between the electrode and the current-collector, electrolyte solution composition, and diffusion of ions in small pores. If redox species/groups are present in the system, such an effect will arise from the resistance of charge transfer due to faradaic phenomena (Pandolfo and Hollenkamp, 2006).

The absence of a redox peak in the CV patterns (Fig. 3) reveals that the contribution of faradaic processes with considerable resistance to charge transfer is negligible. Therefore, the principal contributors to the resistive effects are ionic and electronic conduction through the system. The magnitude of these resistive effects is given by the diameter of the semicircle ($R_p$–$R_s$) of the impedance spectra, where $R_s$ is the resistance of electrolyte and contact resistance between electrode and current collector and $R_p$ is the internal resistance of electrode. The values of these resistances, generally known as ESR = ($R_p$–$R_s$), were obtained from the EIS data for the ACM-K electrodes and are shown in Table 3. The resistive behaviour of these porous electrodes seems to increase with increasing electrode preparation activation time.

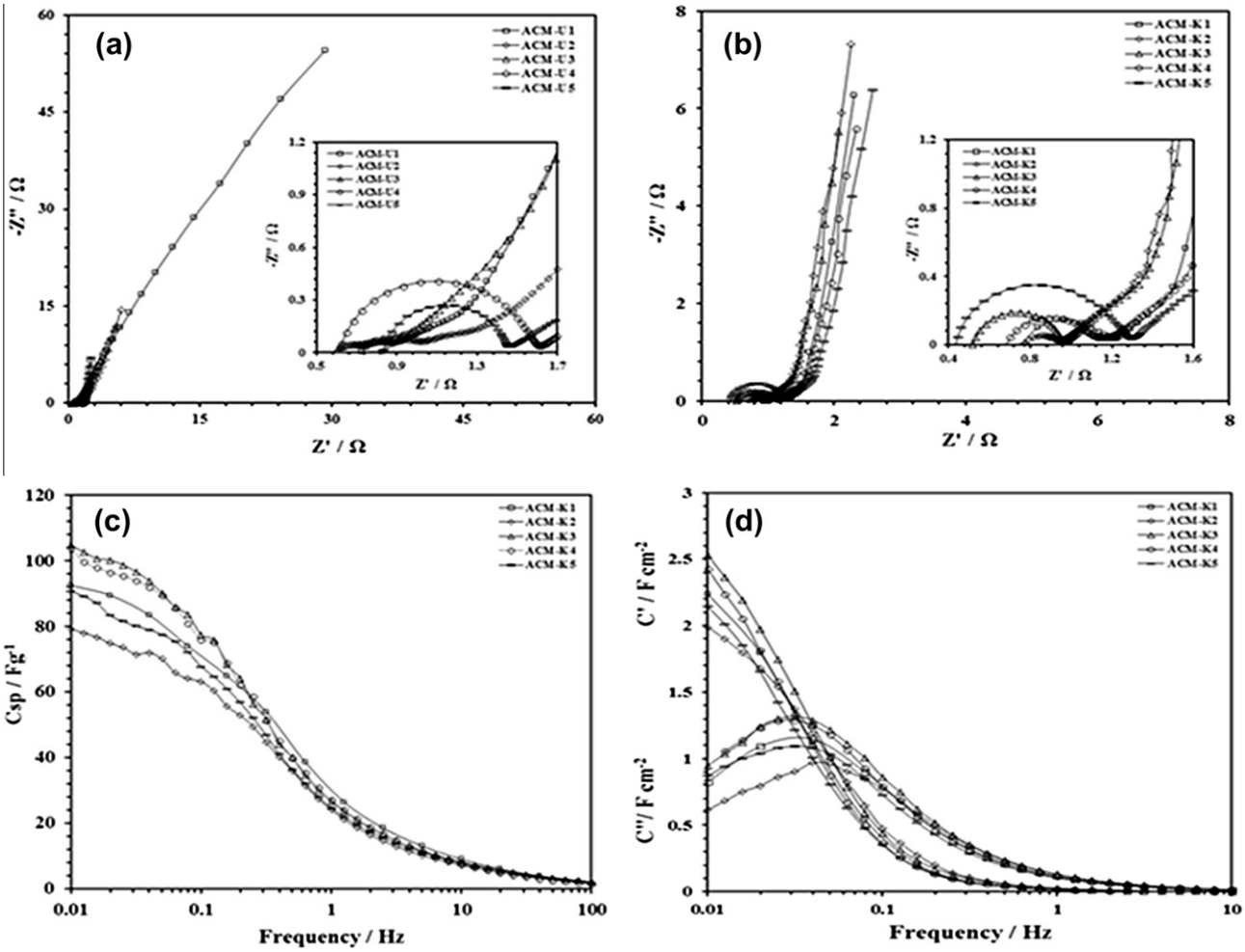


**Fig. 4.** Nyquist plots of (a) ACM-U cells, (b) ACM-K cells (Inset shows expanded versions of impedance plots, (c) specific capacitance for ACM-Ks, and (d). Evolution of imaginary portion and real portion of capacitance versus frequency curves.

The first segment of a straight line in the intermediate frequency region (Warburg region) of the Nyquist plot, shown in Fig. 4(a and b), is commonly found for the microporous carbon electrodes. Its presence is due to the combination of both the resistance of ion migration inside the carbon micropores and the increasing capacitive phenomena that can occur in the pores. In general, a small segment means capacitive phenomena are dominant in the micropores, whereas for a large segment, the resistive effect is relatively more dominant because the real component of impedance continues to increase while the imaginary component significantly deviates from an ideal vertical impedance line. As shown in Fig. 4(b), the first segment of the ACM-K electrodes appears to have almost equal length and slope. Qualitatively, one might assume that this similarity indicates that increases in activation time did not improve ion migration accessibility into electrode micropores in this intermediate frequency range. However, because the position of this segment occurs at a different part of the real axis, one can also assume that this is associated with a different activation time.

All of the impedance curves in Fig. 4(a and b) show the second segment of a straight line in the low frequency region, indicating that the electrically charged electrode/electrolyte interface in the cells exhibits increasing capacitive behaviour. In this low frequency region, the porous structures are penetrated by a greater amount of ionic charges from the electrolyte solution. The accumulation of these charges at the electrode/electrolyte interface may produce the maximum capacitance achievable. The ionic penetration into and accumulation of charges at the available internal surface of porous structure of electrodes are time-dependent processes, as revealed by the slope of this linear segment. The capacitance produced at the electrode/electrolyte interface is a time-dependent parameter; this dependence is described in the following paragraph.

**Table 3**
The values of $R_s$, $R_p$, ESR (EIS), $f_p$ and ESR (GCD) for ACM-Ks cells.

| Cells | $R_s$ (Ω) | $R_p$ (Ω) | ESR (Ω) (EIS) | $f_p$ (Hz) | ESR (Ω) (GCD) |
|---|---|---|---|---|---|
| ACM-K1 | 0.629 | 0.968 | 0.339 | 1995 | 1.008 |
| ACM-K2 | 0.730 | 1.150 | 0.420 | 631 | 1.015 |
| ACM-K3 | 0.534 | 0.961 | 0.426 | 794 | 1.557 |
| ACM-K4 | 0.587 | 1.231 | 0.644 | 316 | 1.633 |
| ACM-K5 | 0.445 | 1.288 | 0.834 | 200 | 1.645 |

The specific capacitance ($C_{sp}$), imaginary capacitance ($C''$) and real capacitance ($C'$) calculated using the standard Eqs. (2), (4) and (5) as a function of frequency cells are shown in Fig. 4(c and d), respectively, for the ACMK-based supercapacitor. As shown in Fig. 4(c), a strong frequency dependence for $C_{sp}$, $C''$ and $C'$ appears in the frequency region below 1 Hz, particularly for the ACM-K3 and ACM-K4 cells. In the low frequency region (below 0.1 Hz), the $C_{sp}$ for ACM-K3 and ACM-K4 are clearly higher than that for other ACM-Ks-based cells, suggesting that activation times of 3–

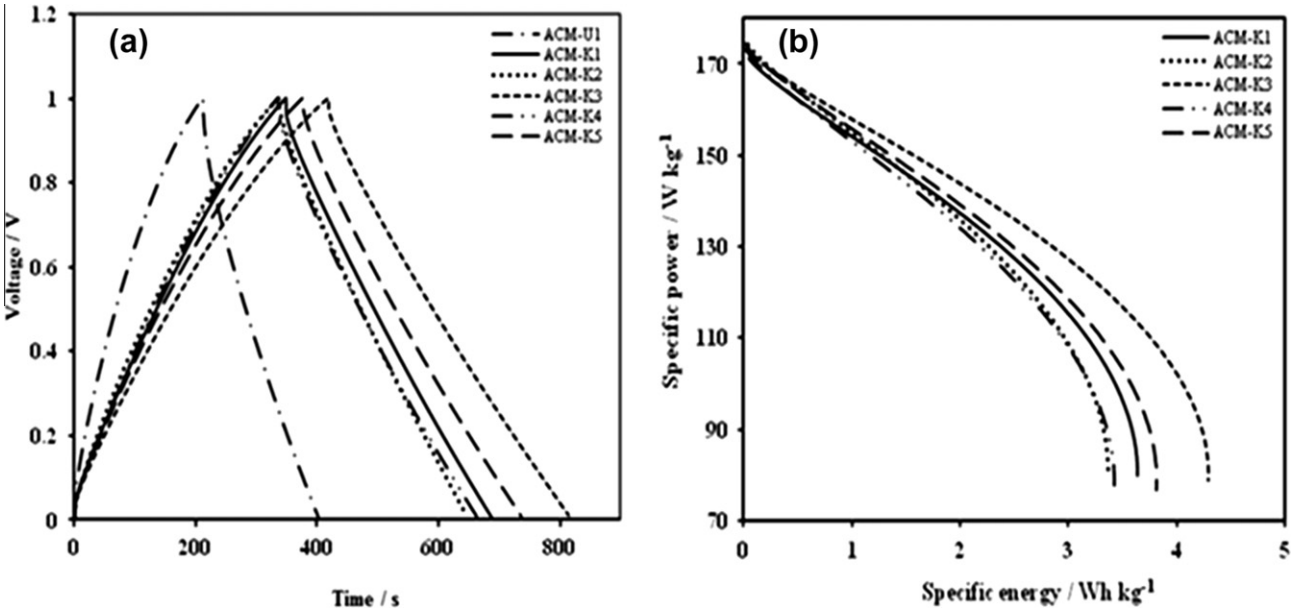


**Fig. 5.** (a) Galvanostatic charge–discharge curves for ACM-U1 cells and ACM-K cells, and (b) Ragone plots for ACM-K-based capacitor cells.

4 h are optimal. For the $C''$ plot, a peak is present at certain values with frequency ($f_p$). The relaxation time constant, $\tau_o$, which defines the boundary between the regions of capacitive and resistive behaviours for the supercapacitor, can be estimated from the equation $\tau_o = 1/f_p$. The calculated $\tau_o$ values for the cells do not show a systematic, strong dependence on the activation. It is well known that higher power delivery corresponds to lower $\tau_o$ values. In the present study, the $\tau_o$ values are comparable to those reported elsewhere (Portet et al., 2005; Pech et al., 2010), suggesting that ACM-K electrodes are suitable electrode materials for higher power delivery.

### 3.2.3. Galvanostatic charge–discharge (GCD)

Fig. 5(a) shows the GCD curves for the ACM-U1 and ACM-K1 to ACM-K5 electrode-based supercapacitor cells. The curve for each electrode has a similar shape, indicating an almost symmetric property resulting from near-equal charge and discharge times. This behaviour indicates that the supercapacitors have electrodes with highly hydrophilic surfaces with very good contact to the electrolyte solution. Despite having a similar shape, the curves differ in their respective charge and discharge times. A comparison of the curves for the ACM-U1 and ACM-K1 electrodes clearly shows the effect of KOH activation on the improvement of charge–discharge efficiency; the latter shows higher charge–discharge time. Further improvement of such efficiency due to an increase in charge–discharge time can be observed for electrodes ACM-K2 to ACM-K5 from their respective curves, which are wider for higher activation times. The wider the base of the curve, the higher the number of electrons and electrolyte ions that become participate during charging and discharging. This expected trend is consistent with the CV and EIS results discussed above (Figs. 3 and 4).

The specific capacitance values of the supercapacitor cells based on the ACM-U1, ACM-K1, ACM-K2, ACM-K3, ACM-K4 and ACM-K5 electrodes were calculated using equation (6) using the data in Fig. 5(a), i.e. 8.6, 120, 127, 150, 129, 135 F $g^{-1}$, respectively. As described qualitatively earlier, these results show a significant combined effect from KOH–$CO_2$ activation. However, for activation times longer than 3 h, specific capacitance decreases. This trend is consistent with the values observed from the EIS and CV data. ESR can also be directly obtained from the data in Fig. 5(a). The value of ESR can be calculated from the sharp voltage drop at the beginning of the discharge curve using the equation ESR = $iR_{drop}/2i$. The values obtained for the ACM-U1 and ACM-K1 to ACM-K5 electrodes are shown in Table 3. In principle, the trend of these val-

**Table 4**
Comparison of $S_{BET}$ and specific capacitance ($C_{sp}$) of electrodes from different biomass precursors.

| Biomass precursor | Activation method | $S_{BET}$ ($m^2$ $g^{-1}$) | $C_{sp}$ (F $g^{-1}$) | Reference |
|---|---|---|---|---|
| Firewood | KOH | 2821 | 95 | Wu et al. (2006) |
| Coffee bean waste | $ZnCl_2$ | 1019 | 368 | Rufford et al. (2008) |
| Cherry stones | KOH | 1624 | 174 | Olivares-Marin et al. (2009) |
| Coffee shell | $ZnCl_2$ | 842 | 156 | Jisha et al. (2009) |
| Recycled waste paper | KOH | 417 | 180 | Kalpana et al. (2009) |
| Cassava peel waste | KOH + $CO_2$ | 1352 | 153 | Ismanto et al. (2010) |
| Sugar cane bagasse | $ZnCl_2$ | 1788 | 300 | Rufford et al. (2010) |
| Apricot shell | NaOH | 2335 | 348 | Xu et al. (2010) |
| Coffee endocarp | $CO_2$ | 709 | 176 | Valante-Nabais et al. (2011) |
| Sunflower seed shell | KOH | 2509 | 311 | Li et al. (2011) |
| Rubber wood sawdust | $CO_2$ | 912 | 138 | Taer et al. (2011) |
| Argan seed shell | KOH | 2062 | 355 | Elmouwahidi et al. (2012) |
| *Camellia olleifera* shell | $ZnCl_2$ | 1935 | 374 | Zhang et al. (2012) |
| Poplar wood | $HNO_3$ | 416 | 234 | Liu et al. (2012) |
| Fibers of palm oil empty fruit bunches | KOH + $CO_2$ | 1704 | 149 | Present study |

ues should be in agreement with those calculated from the EIS data (Kim et al., 2004). It was found that the ESR values from these two different methods are slightly different, but both results exhibit a similar trend.

For comparison with our results, the BET surface area ($S_{BET}$) and specific capacitance of the supercapacitor activated-carbon electrodes prepared via activation methods from various biomass precursors reported in the literature are listed in Table 4. The results for our electrodes (3 h activation) appear to be within the range of the reported results.

### 3.2.4. Specific energy and specific power

The specific power ($P$) and specific energy ($E$) for all of the ACM-K cells, calculated from GCD curves (Fig. 5(a)) using Eqs. (7) and (8), respectively, are shown as Ragone plots in Fig. 5(b). A linear decreasing trend in specific power was observed with increasing specific energy for all cells. The maximum specific energy and specific power were produced by the ACM-K3-based cell, with values of 4.3 Wh $kg^{-1}$ and 173.3 W $kg^{-1}$, respectively. These results fall within the typical range of specific energy and power density for supercapacitors (Simon and Gogotsi, 2008).

## 4. Conclusion

$CO_2$ activation with KOH activating agent was used to process EFB into highly porous binderless carbon monolith electrodes for supercapacitor applications. Supercapacitors based on these electrodes exhibit excellence electrochemical performances due to significantly increased surface area of the electrodes by optimising activation time. This method also has an economic advantage because a very small quantity of KOH can reduce the activation time significantly; consequently preventing excessive heating that can potentially break the monolithic structure of the electrodes during activation. The present study demonstrates an alternative method to conserve chemicals, time and energy during the production of electrodes from biomass residues.

## Acknowledgements

We acknowledge grants from the Universiti Kebangsaan Malaysia (UKM-GUP-216-2011, UKM-DLP-2012-022, UKM-DLP-2012-023), and the support of CRIM (Centre for Research and Innovation Management). The authors also thank Mr. Saini Sain for help with laboratory work.

## References

Awitdrus, Deraman, M., Talib, I.A., Omar, R., Jumali, M.H., Taer, E., Saman, M.H., 2010. Microcrystallite dimension and total active surface area of carbon electrode from mixtures of pre-carbonized oil palm empty fruit bunches and green petroleum cokes. Sains Malaysiana 39, 83–86.

Beidaghi, M., Chen, W., Wang, C., 2011. Electrochemically activated carbon microelectrode arrays for electrochemical micro-capacitors. Journal of Power Sources 196, 2403–2409.

Carrott, P.J.M., Nabais, J.M.V., Ribeiro Carrott, M.M.L., Pajares, J.A., 2001. Preparation of activated carbon fibres from acrylic textile fibres. Carbon 39, 1543–1555.

Chen, H., Wang, F., Tong, S., Guo, S., Pan, X., 2012. Porous carbon with tailored pore size for electric double layer capacitors application. Applied Surface Science 258, 6097–6102.

Coutinho, A.R., Rocha, J.D., Luengo, C.A., 2000. Preparing and characterizing biocarbon electrodes. Fuel Processing Technology 67, 93–102.

Deraman, M., Omar, R., Harun, A.G., Ismail, M.P., 1998. Young's modulus of carbon from self-adhesive carbon grain of oil palm bunches. Journal of Material Science Letter 17, 2059–2060.

Deraman, M., Omar, R., Zakaria, S., Mustapa, I.R., Talib, M., 2002. Electrical and mechanical properties of carbon pellets from acid ($HNO_3$) treated self-adhesive carbon grains from oil palm empty fruits bunch. Journal of Material Science 37, 3329–3335.

Elmouwahidi, A., Zapata-Benabithe, Z., Carrasco-Marin, F., Moreno-Castilla, C., 2012. Activated carbons from KOH-activation of argan (*Argania spinosa*) seed shells as supercapacitor electrodes. Bioresource Technology 111, 185–190.

Fan, S.-P., Zakaria, S., Chia, C.-H., Jamaluddin, F., Nabihah, S., Liew, T.-K., Pua, F.-L., 2011. Comparative studies of products obtained from solvolysis liquefaction of oil palm empty fruit bunch fibres using different solvents. Bioresource Technology 102, 3521–3526.

Ismanto, A.E., Wang, S., Soetaredjo, F.E., Ismadji, S., 2010. Preparation of capacitor's electrode from cassava peel waste. Bioresource Technology 101, 3534–3540.

Jisha, M.R., Hwang, Y.J., Shin, J.S., Nahm, K.S., Kumar, T.P., Karthikeyan, K., Dhanikaivelu, N., Kalpana, D., Renganathan, N.G., Stephan, A.M., 2009. Electrochemical characterization of supercapacitor based on carbon derived from coffee shells. Material Chemistry and Physics 115, 33–39.

Kalpana, D., Cho, S.H., Lee, S.B., Lee, Y.S., Misra, R., Renganathan, N.G., 2009. Recycled waste paper-A new source of raw material for electric double-layer capacitors. Journal of Power Sources 190, 587–591.

Kim, K.-M., Hur, J.-W., Jung, S.-I., Kang, A.-S., 2004. Electrochemical characteristics of activated carbon/Ppy electrode combined with P(VdF-co-HFP)/PVP for EDLC. Electrochimica Acta 50, 863–872.

Kumar, K., Saxena, R.K., Kothari, R., Suri, D.K., Kaushik, K., Bohra, J.N., 1997. Correlation between adsorption and X-ray diffraction studies on viscose rayon based activated carbon. Carbon 35, 1842–1844.

Li, X., Xing, W., Zhuo, S., Zhou, J., Li, F., Qiao, S.-Z., Lu, G.-Q., 2011. Preparation of capacitor's electrode from sunflower seed shell. Bioresource Technology 102, 1118–1123.

Lin, R., Taberna, P.L., Chmiola, J., Guay, D., Gogotski, Y., Simon, P., 2009. Microelectrode study of pore size, ion size, and solvent effects on the charge/discharge behaviour of microporous carbon for electrical double-layer capacitors. Journal of the Electrochemical Society 156, A7–A12.

Liu, M.C., Kong, L.B., Zhang, P., Luo, Y.C., Kang, L., 2012. Porous wood carbon monolith for high-performance supercapacitor. Electrochimica Acta 60, 443–448.

Obreja, V.V.N., 2008. On the performance of supercapacitors with electrodes based on carbon nanotubes and carbon activated material – a review. Physica E: Low-dimensional Systems and Nanostructures 40, 2596–2605.

Olivares-Marin, M., Fernandez, J.A., Lazaro, M.J., Fernandez-Gonzalez, C., Macias-Garcia, A., Gomez-Serrano, V., Stoeckli, F., Centeno, T.A., 2009. Cherry stones as precursor of activated carbons for supercapacitors. Materials Chemistry and Physics 114, 323–327.

Pandolfo, A.G., Hollenkamp, A.F., 2006. Carbon properties and their role in supercapacitors. Journal of Power Sources 157, 11–27.

Pech, D., Brunet, M., Durou, H., Huang, P., Mochalin, V., Gogotsi, Y., Taberna, P.-L., Simon, P., 2010. Ultrahigh-power micrometre-sized supercapacitors based on onion-like carbon. Nature Nanotechnology 5, 651–654.

Portet, C., Taberna, O.L., Simon, P., Flahaut, E., Laberty-Robert, C., 2005. High power density electrodes for carbon supercapacitor applications. Electrochimica Acta 50, 4147–4181.

Razuan, R., Chen, Q., Zhang, X., Sharifi, V., Swithenbank, J., 2010. Pyrolysis and combustion of oil palm stone and palm kernel cake in fixed-bed reactors. Bioresource Technology 101, 4622–4629.

Rufford, T.E., Hulicova-Jurcakova, D., Khosla, K., Zhu, Z., Lu, G.Q., 2010. Microstructure and electrochemical double-layer capacitance of carbon electrodes prepared by zinc chloride activation of sugar cane bagasse. Journal of Power Sources 195 (3), 912–918.

Rufford, T.E., Hulicova-Jurcakova, D., Zhu., Z., Lu, G.Q., 2008. Nanoporous carbon electrode from waste from waste coffee beans for high performance supercapacitors. Electrochemistry Communications 10, 1594–1597.

Simon, P., Gogotsi, Y., 2008. Material for electrochemical capacitors. Nature Material 7, 848–854.

Sing, K.S.W., Everett, D.H., Haul, R.A.W., Moscou, L., Pierotti, R.A., Rouquerol, J., Siemieniewska, T., 1985. Reporting physisorption data for gas/solid systems with special reference to the determination of surface area and porosity. Pure and Applied Chemistry 57, 603–619.

Taer, E., Deraman, M., Talib, I.A., Awitdrus, Hashmi, S.A., Umar, A.A., 2011. Preparation of highly porous binderless activated carbon monolith from rubber wood sawdust by a multi-step activation process for application in supercapacitors. International Journal of Electrochemical Science 6, 3301–3315.

Taer, E., Deraman, M., Talib, I.A., Umar, A.A., Oyama, M., Yunus, R.M., 2010. Physical, electrochemical and supercapacitive properties of activated carbon pellets from pre-carbonized rubber wood sawdust by CO2 activation. Current Applied Physics 10 (4), 1071–1075.

Tsay, K.-C., Zhang, L., Zhang, J., 2012. Effects of electrode layer composition/thickness and electrolyte concentration on both specific capacitance and energy density of supercapacitor. Electrochimica Acta 60, 428–436.

Valante-Nabais, J.M., Teixeira, J.G., Almeida, I., 2011. Development of easy made low cost binderless monolithic electrodes from biomass with controlled properties to be used as electrochemical capacitors. Bioresource Technology 102, 2781–2787.

Wu, F.-C., Tseng, R.-L., Hu, C.-C., Wang, C.-C., 2006. The capacitive characteristics of activated carbons-comparisons of the activation methods on the pore structure and effects of the pore structure and electrolyte on the capacitive performance. Journal of Power Sources 159, 1532–1542.

Xu, B., Chen, Y.F., Wei, G., Cao, G.P., Zhang, H., Yang, Y.S., 2010. Activated carbon with high capacitance prepared by NaOH activation for supercapacitors. Materials Chemistry and Physics 124, 504–509.

Zhang, J., Gong, L., Sun, K., Jiang, J., Zhang, X., 2012. Preparation of activated carbon from camellia oleifera shell for supercapacitor application. Journal of Solid State Electrochemistry 16 (6), 2179–2186.

Zhang, L.L., Zhao, X.S., 2009. Carbon-based materials as supercapacitor electrodes. Chemical Society Reviews 38, 2520–2531.

Zhao, N., He, C., Jiang, Z., Li, J., Li, Y., 2007. Physical activation and characterization of multi-walled carbon nanotubes catalytically synthesized from methane. Material Letters 61, 681–685.